We are IntechOpen, the world's leading publisher of Open Access books Built by scientists, for scientists

6,900
Open access books available

185,000
International authors and editors

200M
Downloads

154
Countries delivered to

Our authors are among the

TOP 1%
most cited scientists

12.2%
Contributors from top 500 universities

WEB OF SCIENCE™

Selection of our books indexed in the Book Citation Index
in Web of Science™ Core Collection (BKCI)

Interested in publishing with us?
Contact book.department@intechopen.com

Numbers displayed above are based on latest data collected.
For more information visit www.intechopen.com

Heat Transfer Analysis without and with Forward Facing Spike Attached to a Blunt Body at High Speed Flow

Rakhab Chandra Mehta

Additional information is available at the end of the chapter

Abstract

The present chapter deals with heat transfer analysis around unspiked and spiked bodies at high speeds. A spike attached to a blunt-nosed body drastically alters its flowfield and influences the aerodynamic heating in a high speed flow. The effect of spike length, shape and spike-nose configuration is numerically studied at zero angle of incidence. The numerical analysis describes overall flowfield features over without and with forward facing spike attached to a blunt body at high speed flow. The shock stand-off distance, sonic line, stagnation point velocity gradient and stagnation point heat flux are analyzed and compared with different aerodisk configurations. It is found that the hemispherical aerodisk experiences high wall heat flux as compared to the flat-faced aerodisk. Numerical and experimental studies reveal that the wall heat flux levels are decreased in the presence of the spikes and aerospike as compared to without attached spiked to the blunt-nose basic configuration.

Keywords: aerospike, blunt body, CFD, compressible flow, convective heat transfer

1. Introduction

The shock wave dominates aerodynamic drag and aerodynamic heating at high speeds of a blunt body. The analytical [1] and experimental [2] investigations have shown that for the blunt body noses with a fixed length, a pointed geometry with a blunt nose tip is most beneficial to minimize the wave drag at high speeds. If aerodynamic heating is considered, a large blunt nose radius R_N is preferred since the wall heat flux, q_w, is reciprocally proportional to the square root of R_N [3]. A blunt nose [4] is beneficial in increasing the volumetric space to accommodate more payload and avionic components in a space vehicle.

There are several alternative concepts to the aerospike developed such as changing catalyst properties [5], pulse heating in front of the blunt body [6–8], DC arc discharging [9], electrically heated wire pointing upstream [10], injection of jets of air [11–13], or plasma technology [14–16], forward facing cavity [17], self-aligning aerodisk [18], opposite jet injection [19], focused energy deposition [20–22], non-ablative thermal protection [23] and multiaerodisk attached to the blunt body [24]. Many review articles have appeared [25–27] to summarize the flowfield characteristics in front of the blunt body to the aerospike.

The features of the high speed flowfield can be delineated through these experimental [28] and numerical [29, 30] studies. Based on these investigations a schematic of the flowfield around the blunt body, the conical, the hemispherical and the flat-face spiked blunt body at zero angle of incidence is delineated in **Figure 1**. A hemi-spherical portion of the blunt body is accomplished by a bow shock wave as depicted in **Figure 1(a)**. The total pressure loss over the shock leads to a high wave drag. A well-known concept for reducing the impact of the bow shock wave on a blunt body, while keeping a blunt nose, is the aerospike. The simplest aerospike design is a thin rod mounted on the tip of a blunt body as in **Figure 1(b)**. For the aerospike in ideal case, the boundary layer on the rod separates along the whole rod surface due to the pressure rise over the bow shock wave [31]. The separated boundary layer forms a shear layer that is reattached on the blunt nose. Due to the shear layer, the outer supersonic bow is detected and a weaker conical shock is formed instead of the initial bow shock. The conical shock unites with the reattachment shock further downstream. A recirculation zone forms inside the shear surface and shows significantly lower pressure levels compared with the blunt body without an aerospike. In the model of the flat-face and the hemispherical aerodisk, we observe a formation of a bow shock wave ahead of the body as delineated in **Figure 1(c)** and **(d)**. The flow separation zone is noticed around the root of the spike up to the reattachment point of the flow at the corner of the blunt body. Due to the recirculating region, the pressure at the stagnation region of the blunt body will reduce.
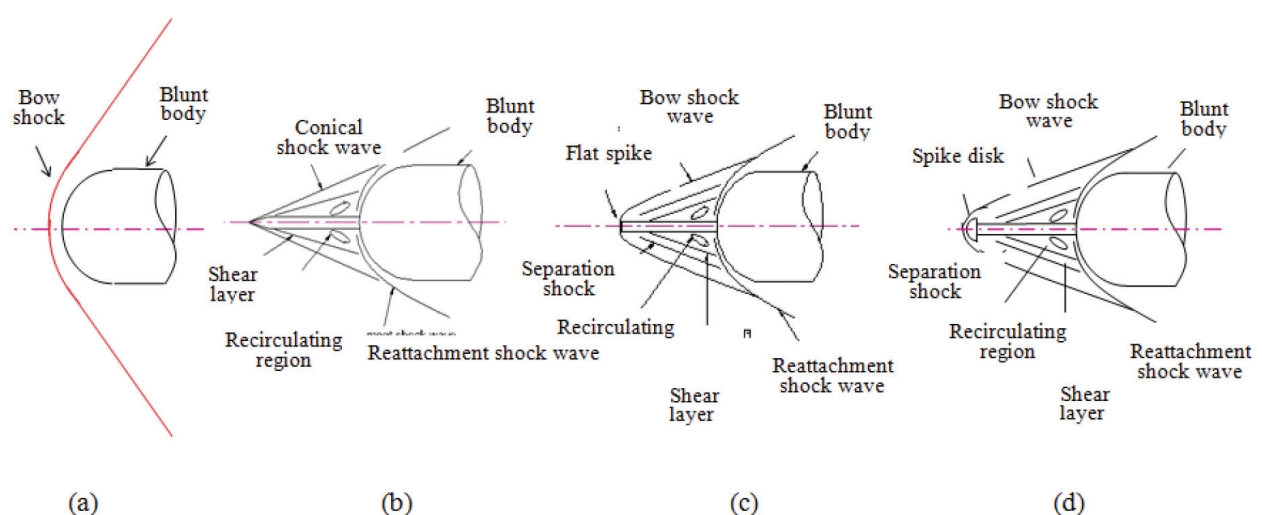

Figure 1. Flowfield features around unspiked and spiked bodies at high-speeds: (a) blunt body (b) conical spike (c) flat-face spike and (d) hemispherical disc spike.

However, because of the reattachment of the shear layer on the corner of the blunt body, the pressure near the reattachment point becomes large. However, the reattachment point can depend on the geometrical parameters of the spike or the blunt body configuration. The spike is characterized by a free shear layer, which is formed as a result of the flow separating from spike leading edge and reattaching to the blunt body, essentially bridging the spike. The separating shear layer from the spike leading edge of the aerospike attaches to the blunt body, after entering through an expansion fan at the leading edge corner and a recompression shock at attachment point. The attached shear layer then separates near the trailing edge and generates a separation shock before reattaching point at the trailing edge prior to undergoing flow expansion. The separated boundary layer forms a shear layer that reattaches on the blunt nose.

The above descriptions of the flowfield features show that the flowfield past a spiked blunt body appears to be very complicated and complex and having a number of interesting flow phenomena and characteristics, which have been further studied in order to compute the aerodynamic heating at high speeds.

2. Governing equations

The time-dependent axisymmetric compressible fluid dynamics equations were written in integral form, and the system of equations was augmented by the ideal gas law for numerical simulation [31]. The coefficient of molecular viscosity was calculated using Sutherland's law. A laminar flow is considered in the numerical simulation which also agrees with Bogdonoff and Vas [32], Fujita and Kubota [33], Yamauchi et al. [34] and Ahmed and Qin [25].

3. Numerical algorithm

The flowfield solver uses a finite-volume discretization employing the method of lines. The spatial computational region was divided into a number of finite non-overlapping quadrilateral grids. Thus, the discretized solution to the Navier-Stokes equations results in a set of volume-averaged state variables of mass, momentum and energy, which are in balance with their area-averaged fluxes (inviscid and viscous) across the grid faces [35]. The finite-volume flow solver algorithm written in this way reduces to a central difference scheme and is second-order accurate in space provided that the grid is generated in an orderly manner and is smooth enough. The cell-centered spatial discretization method is non-dissipative [36]; therefore, artificial dissipation terms are added as a blend of a Laplacian and biharmonic operator in an analogous to the second and fourth difference. The artificial dissipation term was added in the algorithm explicitly to prevent numerical oscillations near flow discontinuity to dampen high-frequency undamped modes. Temporal integration was performed using a multistage time-stepping scheme of Jameson et al. [36] and numerical integration used on the Runge–Kutta method. The artificial dissipation is evaluated only at the first stage.

3.1. Initial and boundary conditions

An initial condition corresponding to freestream conditions is considered. All flow quantities were extrapolated at the outer-boundary, and the no-slip condition was imposed on the wall. An isotherm wall condition was used for the wall of the model, that is, a surface temperature of 300 K. The symmetric condition is imposed on the centerline.

3.2. Computational grid

One of the controlling factors for the numerical simulation is the proper grid arrangement. The grid points are generated by a homotopy scheme [37]. Mesh-independence tests were performed, taking into consideration the influence of the computational region, the stretching factor to control the mesh intensity in the vicinity of body surface and the number of mesh points in the axial and normal directions. The outer surface of the computational zone is varied about 5–8 times the maximum blunt body diameter D. the mesh stretching factor in the radial direction is varied in order to resolve boundary layer. The convergence criterion is based on the difference in density value at any grid point between two successive iterations, that is, $|\rho^{n+1} - \rho^{n}| \leq 10^{-5}$, where n is the iteration index.

4. Geometrical details of model

4.1. Axisymmetric blunt body

The spherical blunted-cone/flare configuration without spike is illustrated in **Figure 2(a)**. The spherical forebody has $R_N = 0.51$ m, $D = 2.03$ m, $L = 1.67$ m, and cone angle of $20°$. The flare has a semi-cone angle $15°$ and is terminated with a right circular cylinder. A close-up view of the computational mesh is shown in **Figure 2(b)**.
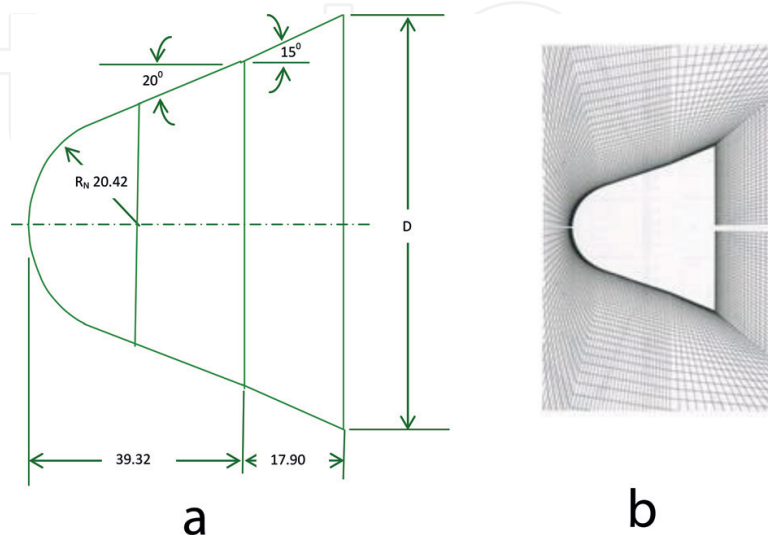

Figure 2. (a) Geometrical parameters of reentry capsule and (b) enlarged view of computational grid.

4.2. Heat shield with forward facing spike

The fore and afterbody diameters of the heat shield [38–39] are 43.26×10^{-3} and 35×10^{-3} m, respectively, as shown in **Figure 3(a)**. The semi-cone angle of the heat shield is 20°. The hemispherical nose of the forward facing spike has radius of 0.55×10^{-3} m and length of the spike is 10×10^{-3} m. The other end of spike has diameter of 0.98×10^{-3} m and is attached to the blunt spherical cap of the heat shield of radius 8.75×10^{-3} m. The computational grid is displayed in **Figure 3(b)**.

4.3. Conical spike attached to blunt body

The model is axisymmetric, the main body has a hemisphere-cylinder nose and diameter $D = 7.62 \times 10^{-2}$ m. The spike's stem has a conical and cylindrical shape. The angle of the spike's cone is 10° and diameter of the cylinder of the spike is 0.1D. Length to diameter ratio of spike are considered as 0.5, 1.0 and 2.0 in the flowfield and heat transfer analysis. **Figure 4(a)** depicts the geometrical dimensions and enlarged view of mesh over the model in **Figure 4(b)**.
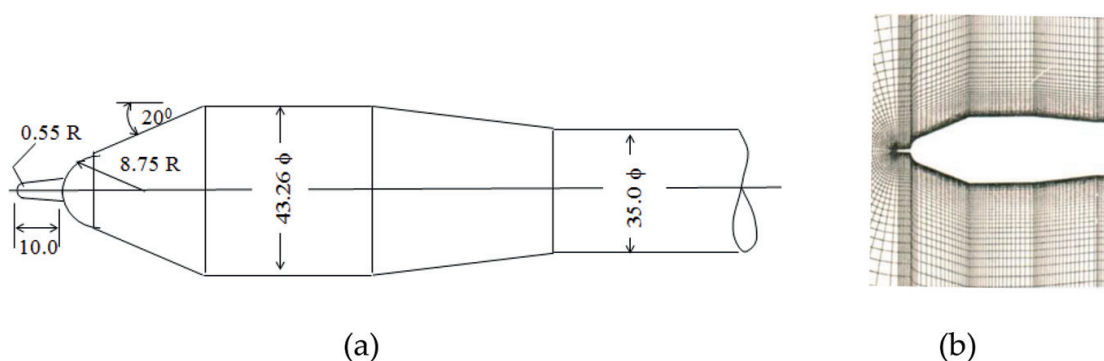

(a) (b)

Figure 3. (a) Dimensions of the heat shield with spike and (b) enlarged view of the grid.
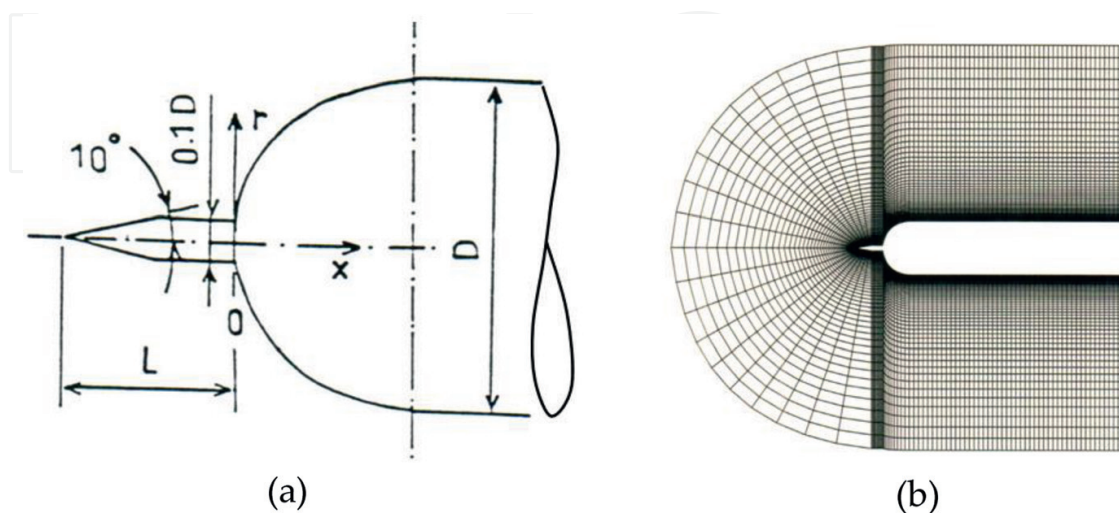

(a) (b)

Figure 4. (a) Dimensions of the spiked blunt body and (b) computational grid.
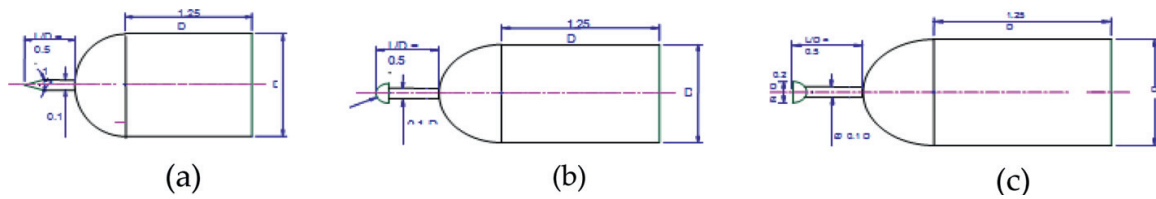
Figure 5. Dimensions of the aerospike blunt bodies: (a) conical spike (b) hemispherical spike and (c) flat-face disc.
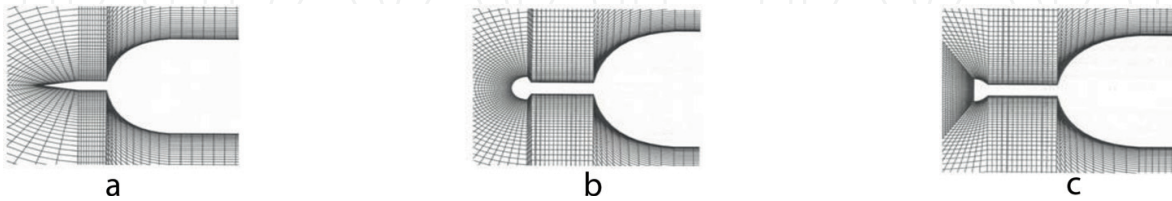

Figure 6. Close-up view of computational grid over the aerospike blunt bodies: (a) conical spike (b) hemispherical spike and (c) flat-face disc.

4.4. Conical, disk and flat spiked body

The dimensions of the spiked blunt body are depicted in **Figure 5**. The basic body has a hemispherical-cylinder nose and diameter $D = 4.0 \times 10^{-2}$ m. The conical spike is as shown in **Figure 5(a)**. The semi cone is 15°, the spike length $L = 0.5$ D and stem diameter of 0.1 D. The spike having a hemispherical cap of diameter D_s is 0.2 D, attached to a stem of diameter of $0.1D$. The aerodisk type configuration utilizes a hemispherical disk on its nose of diameter D_s is $0.2D$ as depicted in **Figure 5(b)**. The flat-faced aerodisk with spike length $L = 0.5$ D is shown in **Figure 5(c)**. A close-up view of the computational grid over the conical, the hemispherical and the flat-faced aerospike is depicted in **Figure 6**. The structured grid generation and the mono-block are suitable to accommodate aerospike shape.

5. Results and discussions

Characteristic features of the flowfield around the hemispherical and the flat-disk aerospike attached to the blunt body at high speeds were investigated with the help of velocity vector plots, density, pressure and Mach contours diagram.

5.1. Flow and heat transfer analysis of axisymmetric blunt body

Computed Mach and temperature contours around the unspiked reentry module are shown in **Figure 7** for M_∞ = 2.0–6.0. The Mach contours exhibit the vortices formation at the shoulder region of the module. Behaviors of the flowfield around the blunt body at supersonic speeds shows the formation of the bow shock wave ahead of the blunt body; the wake, and the recompression shock waves coming out from the neck point are observed in the Mach contours. The flow expands at the base region and is followed by the recompression shock downstream of the base. Then, the flow progress in the wake region. The flow ground of the capsule is divided
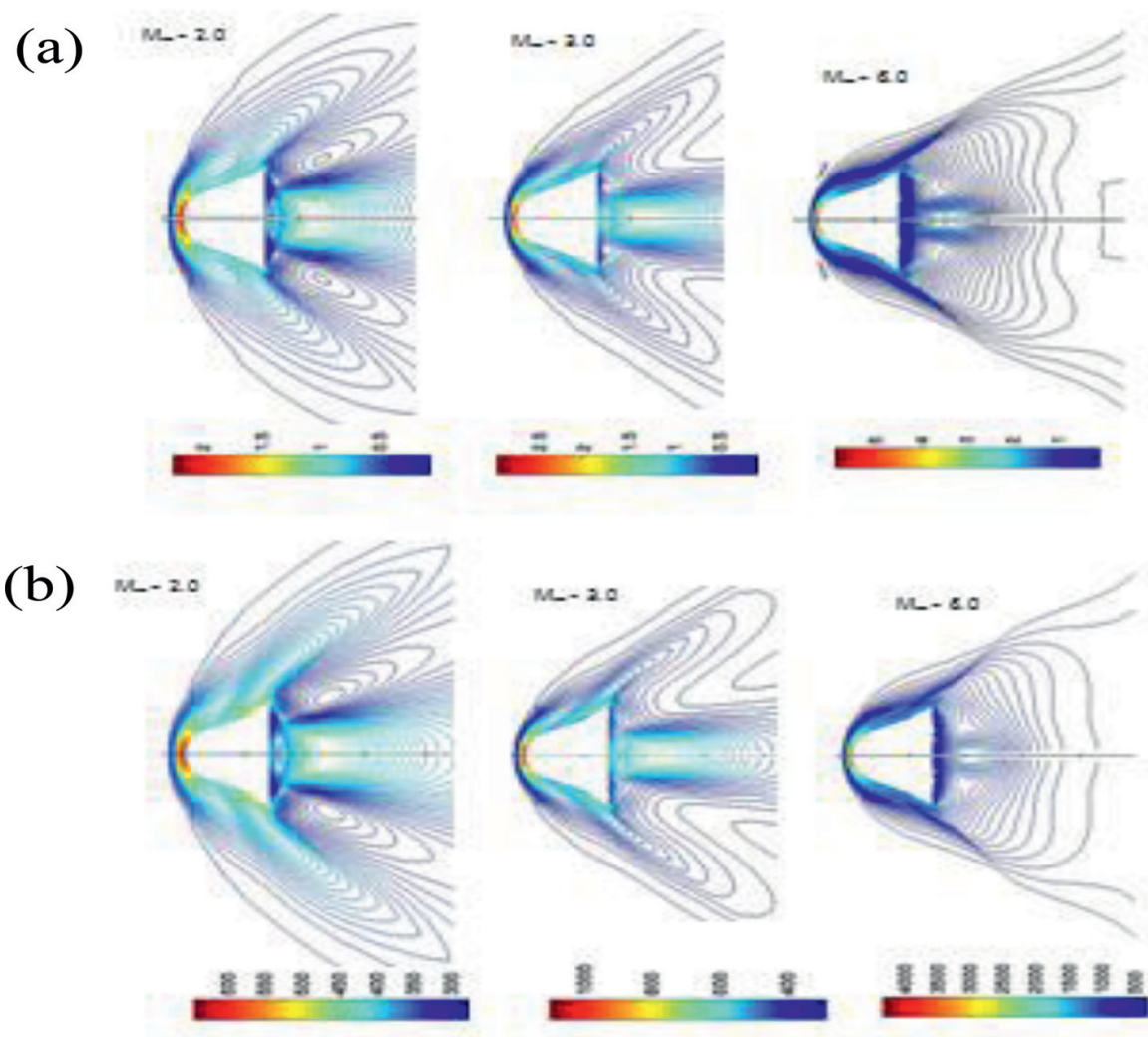
Figure 7. (a) Mach and (b) temperature contours over the blunted-cone/flare module.

into regions inside and outside of the flow recirculation zone, and two flow zones are separated by the shear layer. From the temperature contours, a rapid raise of temperature with the increase of M_∞ can be observed.

Figure 8 shows the pressure coefficient [$Cp = 2\{(p/p_\infty)-1\}/\gamma M_\infty^2$] and wall heat flux q_w variation along the surface of the reentry module for $M_\infty = 2.0$–6.0. The $s/D = 0$ location is the stagnation point, where s is the distance taken along the surface of the blunt body from the stagnation point and D is the maximum diameter of the module. The pressure coefficient on the spherical cap of the capsule decreases gradually for a given M_∞. It can be visualized from **Figure 8(a)** that the Cp falls on the sphere-cone junction and remains constant over the cone. A sudden drop in Cp is observed on the shoulder of the module followed by a negative Cp variation in the base flow region. A low pressure is occurred immediately downstream of the base of the module which is characterized by a low speed recirculating flow region. In the base region, Cp is decreases with increasing M_∞. The variation of wall heat flux along the body is shown in **Figure 8(b)**. The wall heat flux q_w distribution along the wall shows similar characteristics as the pressure coefficient variation and q_w increases with increasing M_∞.
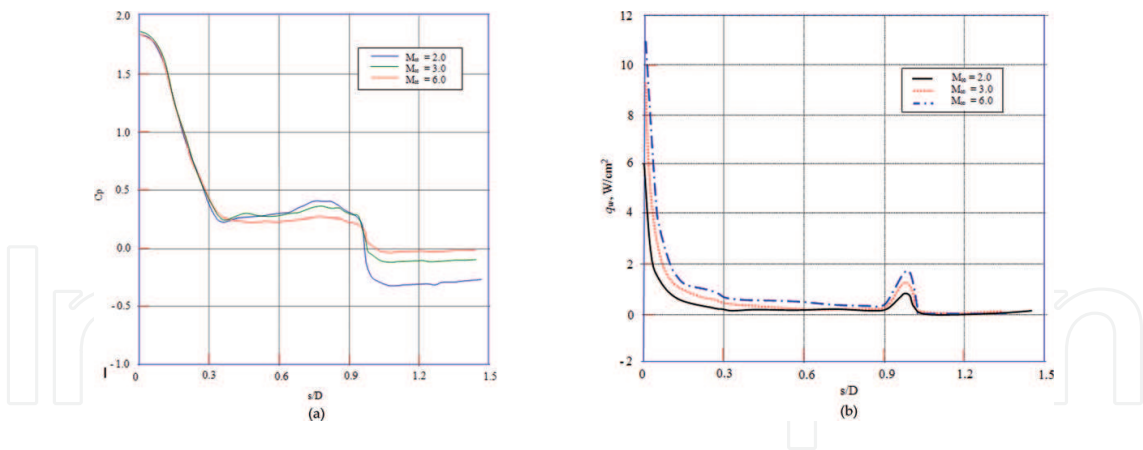
Figure 8. Variation of (a) pressure coefficient and (b) wall heat flux over reentry module.

5.2. Heat shield with a forward-facing spike

Figure 9 depicts the close-up view of the velocity vector plots and Mach contours unspiked and spiked over the heat shield [39]. We can visualize from the vector plot in **Figure 9(a)** the interaction between bow shock wave and reattachment shock. The recirculation region behaves as if it has a spike boundary. A significant flowfield is found around the unspiked and spiked heat shield as depicted in **Figure 9(b)**. **Figure 10** depicts the surface pressure coefficient and wall heat flux variation along blunt body surface for $M_\infty = 2.0$. A very high-pressure peak can be seen in the Cp variation. The wall heat flux variation along the model exhibits similar characteristics as the Cp variation. The peak in the heat flux is found at about the same location as in the Cp distribution.

5.3. Conical spike attached to the blunt body

Interaction between the conical oblique shock wave starting from the tip of the spike and the reattachment shock wave of blunt body is observed in the pressure, density and Mach contours in **Figure 11**. The reflected reattachment wave and shear layer from the interaction are shown behind the reattachment shock wave. A large separated region is found in front of the blunt body and the shear layer, the boundary of the separated region is
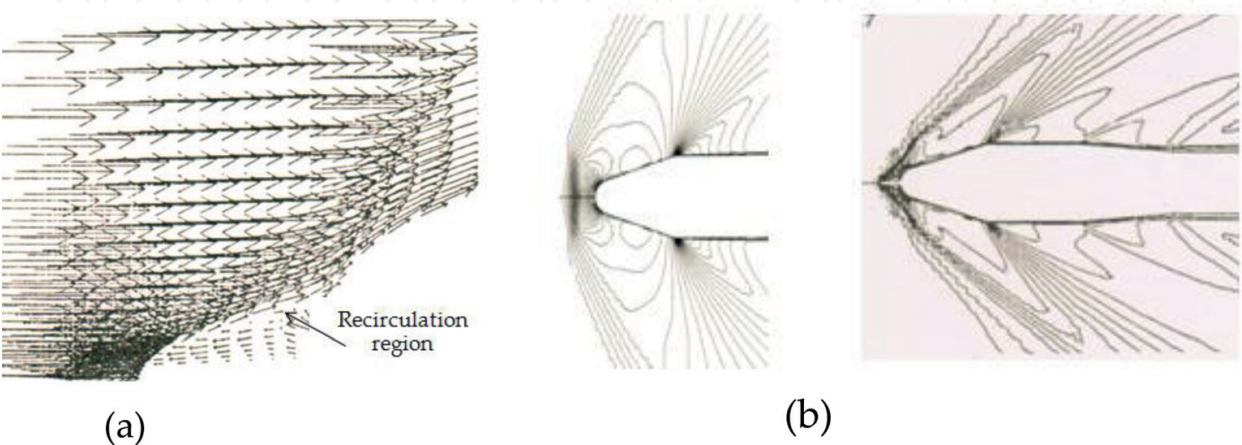
Figure 9. (a) Velocity vector and (b) Mach contours over the heat shield at $M_\infty = 2.0$.

a

b
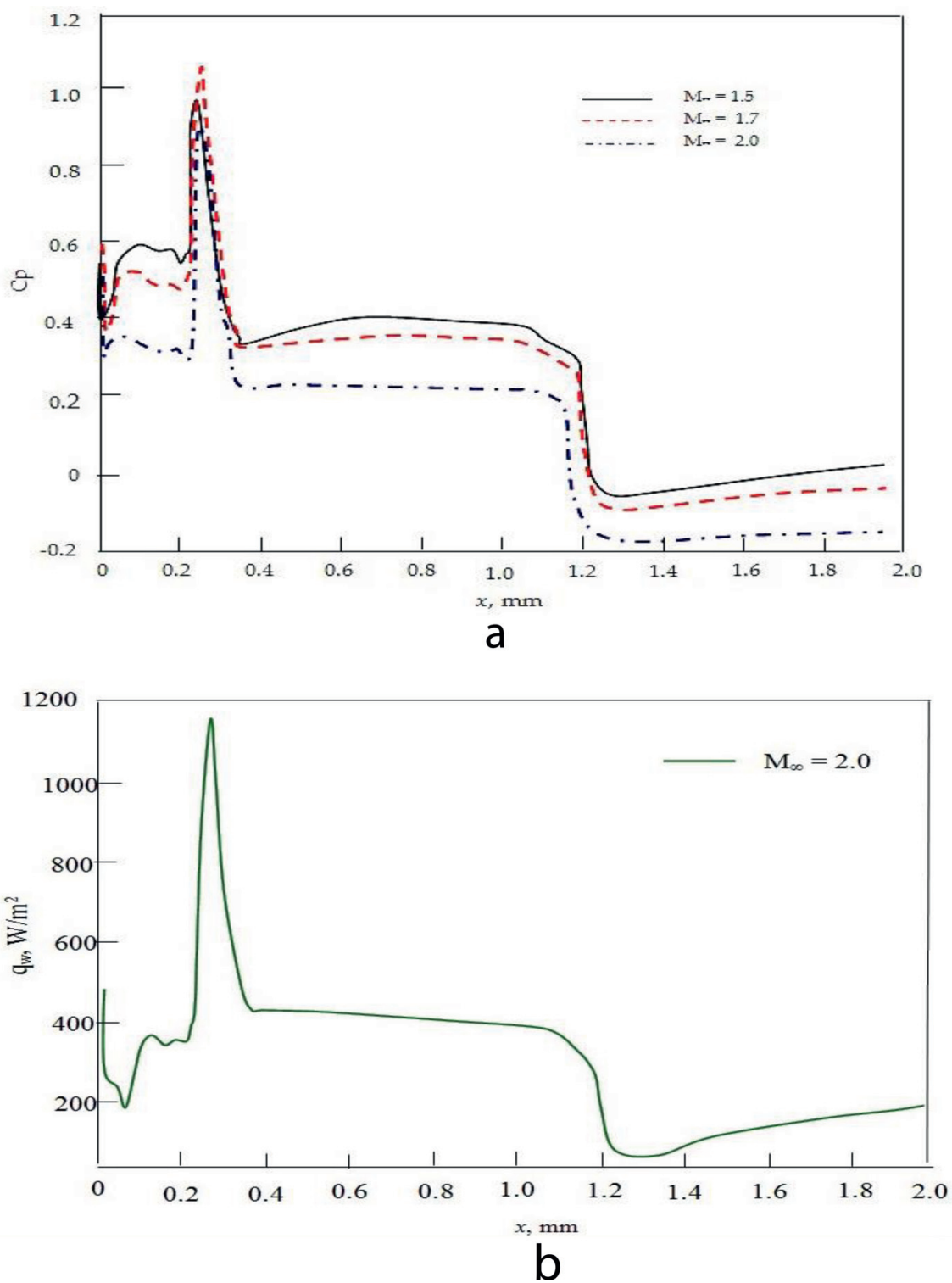
Figure 10. Variation of (a) pressure coefficient and (b) wall heat flux over the spiked heat shield.

visible. The variation of p/p_∞ and q_w along the spike blunt body is shown in **Figure 12(a)** and **(b)**, respectively. A sharp and sudden rise of heat flux is noticed very close to the spike tip, which is attributed to flow stagnation. The secondary peak heat flux is seen at about the reattachment point.

Figure 11. Contour plots over the spiked blunt body: (a) pressure (b) density and (c) Mach number.

5.4. Conical, disk and flat attached to the blunt body

5.4.1. Shock stand-off distance

The computed density contour plots over the conical, the hemispherical and the flat-faced aerospiked configurations are shown in **Figure 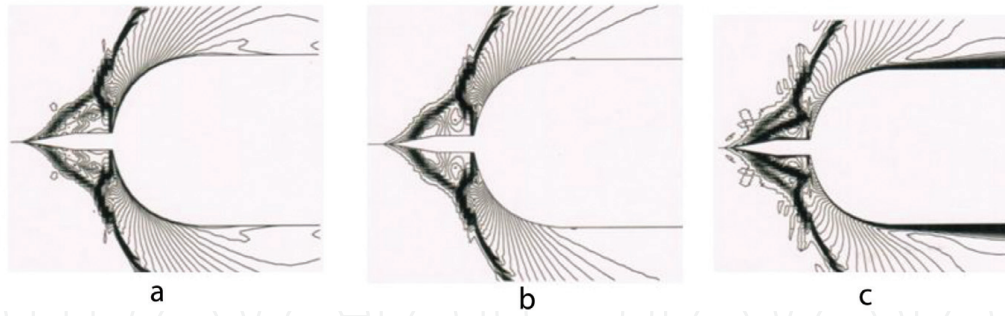13(a), (b)** and **(c)**, respectively. The separated shear layer and the recompression shock from the reattachment point on the corner of the unspiked blunt body are observed in the flowfield region of contour diagram. The bow shock wave in front of the aerospike disk will decrease the aerodynamic drag as compared to the case the unspiked body as observed in the contour plots. In the fore-region of the aerodisk, the flow velocity decreases after the bow shock wave. At the corner of the aerodisk, the flow turns and expands rapidly, the boundary layer separates, gives a free-shear layer that separates the recirculating flow zone after the base region to the outer region. For the case of a button type spike flying at hypersonic speeds, a detached bow shock wave is observed in front of the spike which is appeared normal at to the body axis [29]. Since the flow behind the normal shock is subsonic, simple continuity considerations may show that the shock-detachment distance and stagnation-velocity gradient are essentially a function of ρ_2/ρ_∞ across the normal shock. The flow behind the bow shock wave is subsonic; the flow is no longer independent of the far-downstream influences. An alteration of the spike geometry in the subsonic region alters the complete flowfield up to the bow shock wave. **Figure 14(a)** shows schematic bow shock stand-off distance and the position of the sonic line. A schematic sketch of the bow shock stand-off distance of the flat-faced and the hemispherical spike attached to the blunt body is shown in **Figure 14(b)** and **(c)**. The bow shock-detachment distance becomes smaller with increasing ρ_2/ρ_∞. Probstein [40] gives an expression for the shock detachment distance Δ_F (**Figure 14(b)**) with diameter of the flat-disk D_S radio as:

$$\frac{\Delta_F}{D_S} = 2.8\sqrt{\frac{\rho_\infty}{\rho_0}} \tag{1}$$

The gas is considered thermally and calorically perfect. The ratio of the flow properties across the normal shock wave [41, 42] can be calculated as a function of M_∞ and γ, the relations are

$$\frac{\rho_2}{\rho_\infty} = \frac{(\gamma+1)M_\infty^2}{(\gamma-1)M_\infty^2 + 2} \tag{2a}$$
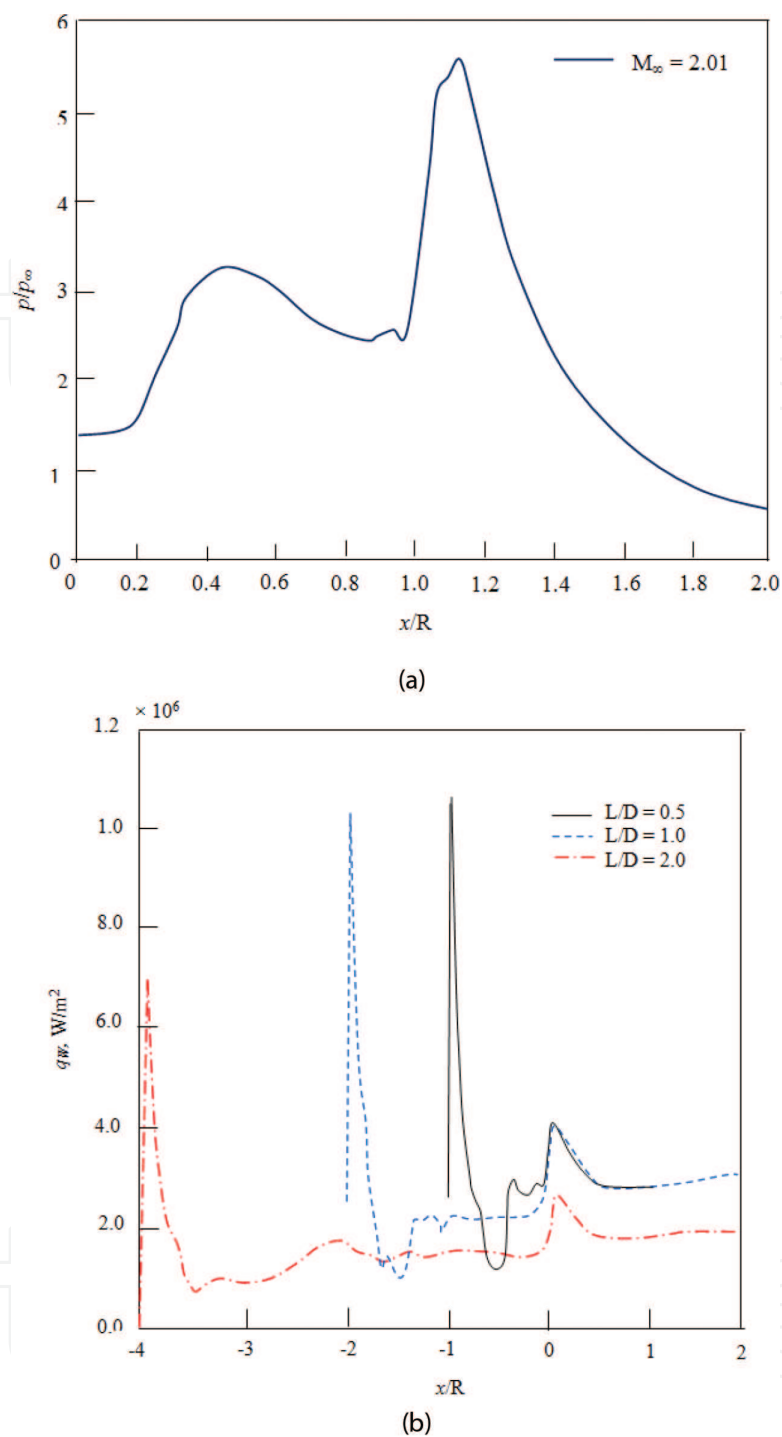
Figure 12. Variation of (a) pressure ratio and (b) wall heat flux over the spiked blunt body.

$$\frac{\rho_e}{\rho_\infty} = \frac{(\gamma+1)M_\infty^2}{(\gamma-1)M_\infty^2+2}\left[1+\frac{\gamma-1}{2}\frac{(\gamma-1)M_\infty^2+2}{2\gamma M_\infty^2-\gamma+1}\right]^{1/(\gamma-1)} \tag{2b}$$

$$\frac{p_e}{p_\infty} = \left[\frac{(\gamma+1)M_\infty^2}{2}\right]^{\gamma/(\lambda-1)}\left[\frac{\gamma+1}{2\gamma M_\infty^2+(\gamma-1)}\right]^{1/(\lambda-1)} \tag{2c}$$
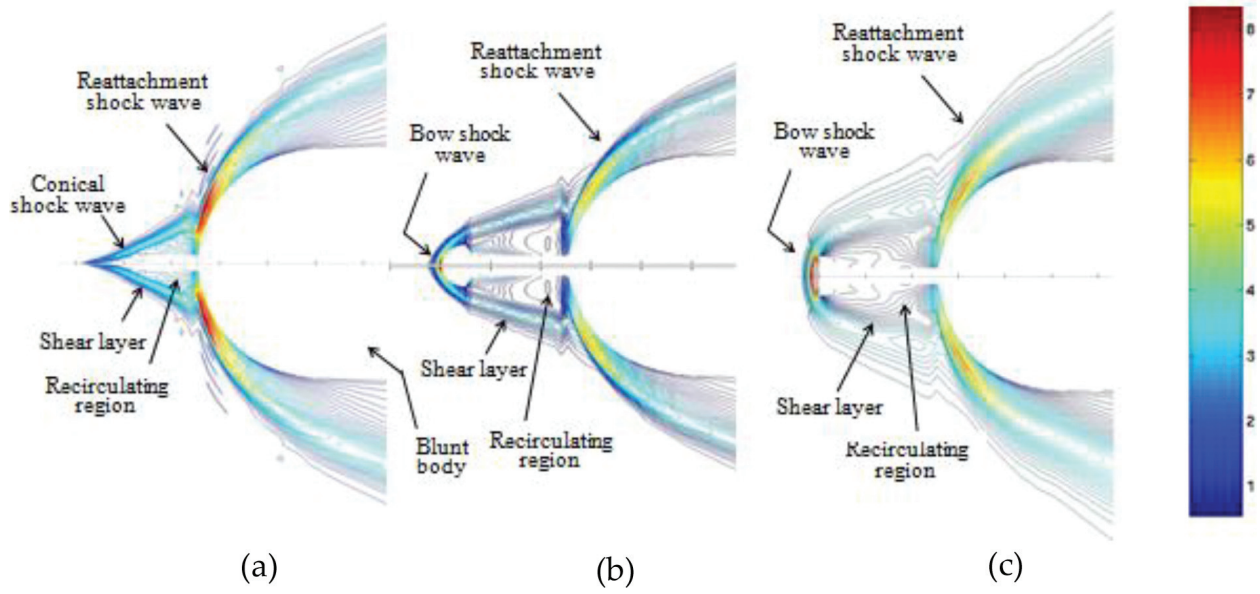
Figure 13. Mach contours over (a) the conical spike (b) the hemisphere and (c) flat-faced aerospike attached to the blunt-body.

The effects of the subsonic flow on the hemispherical and the flat-face disk bodies have been investigated by Truitt [43]. The nomenclature is illustrated in **Figure 14(a)**. The freestream flow passes through the normal portion of the shock wave reaching state *2* then decelerates isentropically to state *e*, which constitutes the edge condition for the thermal boundary layer at the stagnation point. The ratio of shock stand-off distance Δ_S with hemispherical spike of diameter, D_S (**Figure 14(c)**) is

$$\frac{\Delta_S}{D_S} = \frac{2\left(\frac{\rho_\infty}{\rho_0}\right)}{1 + \sqrt{\frac{8\left(\frac{\rho_\infty}{\rho_0}\right)}{3}}} \tag{3}$$

The values of Δ_F/D_S and Δ_S/D_S are found to be 0.1898 and 0.1109, respectively. The spherical spike shows the greatest change in velocity gradient as compared to the flat-face disk. The flow is compressed to subsonic condition, which appears as inviscid and incompressible [44]. The shock wave stands in front of the blunt body and forms a region of subsonic flow around the stagnation region. The bow shock wave stand-off distance is calculated employing the following asymptotic formula of Frank and Zierep [45]:

$$\frac{\Delta}{R_N} = \frac{2(b)^{2/3}}{\left[\frac{(M_\infty^2 - 1)}{(\gamma+1)M_\infty^2}\right]^{2/3}} - 1 \tag{4}$$

where the value of b is taken as 0.14 [45]. The bow shock stand-off distance Δ/R_N is 0.17. The present numerical data is in agreement with the experimental data [46], asymptotic formula of Frank and Zierep [45] and with the theoretical results of Van Dyke and Gordon [47].
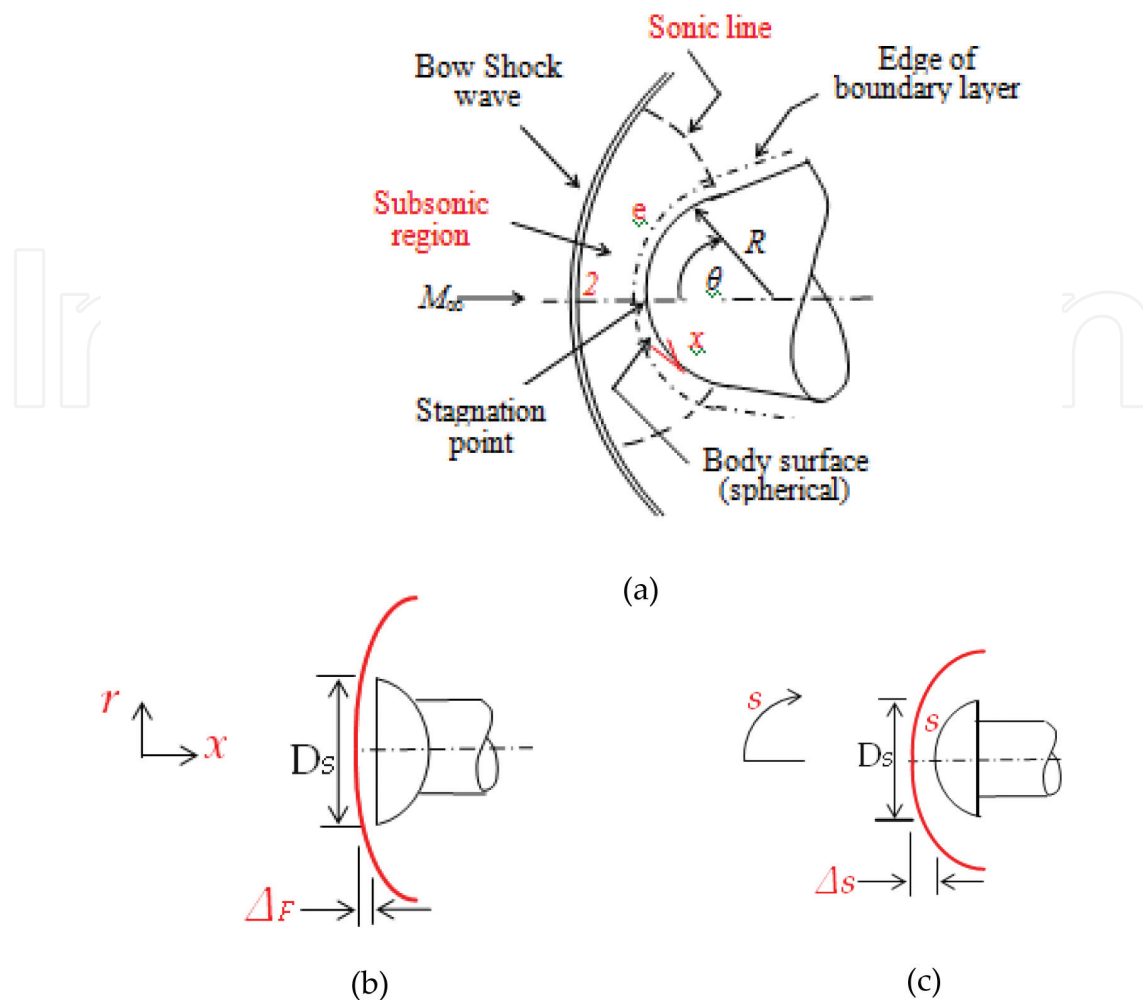
Figure 14. (a) Schematic sketch of flowfield over the blunt body, (b) the hemisphere and (c) the flat-face disc spiked.

5.4.2. Surface pressure variations

The pressure coefficient distribution on the spiked blunt-body with other aerospikes configu-
rations is given in **Figure 15**. The $x/R = 0$ is the location of the spike tip, where R is radius of the
blunt body. The maximum pressure on the surface of the spiked blunt body is found at an
angle of about $40°$. This is the point of flow reattachment. It is interesting to notice that the
maximum pressure is obtained on the same location on the hemisphere body. The low-
pressure region in front of the body attributes reason for the drag reduction.

Tables 1 and **2** depict the variation of pressure coefficient, non-dimensional pressure, skin
friction coefficient and wall heat flux over the spike surface facing the flow direction along the
spike. The $s/D_S = 0$ is measured from the stagnation point. The s is location along the surface of
spike and D_S is diameter of the spike as shown in **Figure 14(b)** and **(c)**. The p/p_∞ on the
stagnation point is 38.23 and 48.84 for the flat-disk aerospike and the hemispherical disk
aerospike, respectively. The pressure ratio across the normal shock is 41.83. It shows the
percentage p/p_∞ difference of the order of -8.59% and 16.77% for the flat-disk and the hemi-
spherical disk aerospike, respectively. The difference is attributed to the finite compressibility
in the shock and the spike surface.
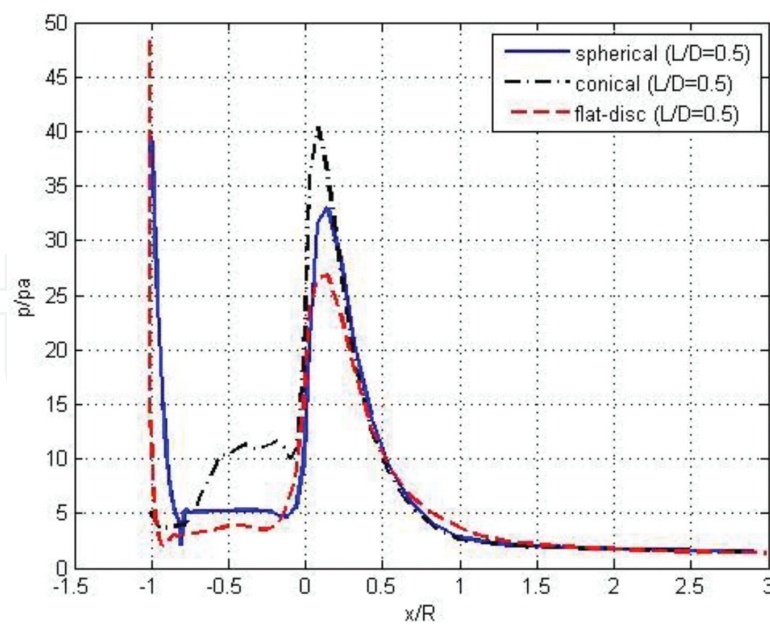
(a)
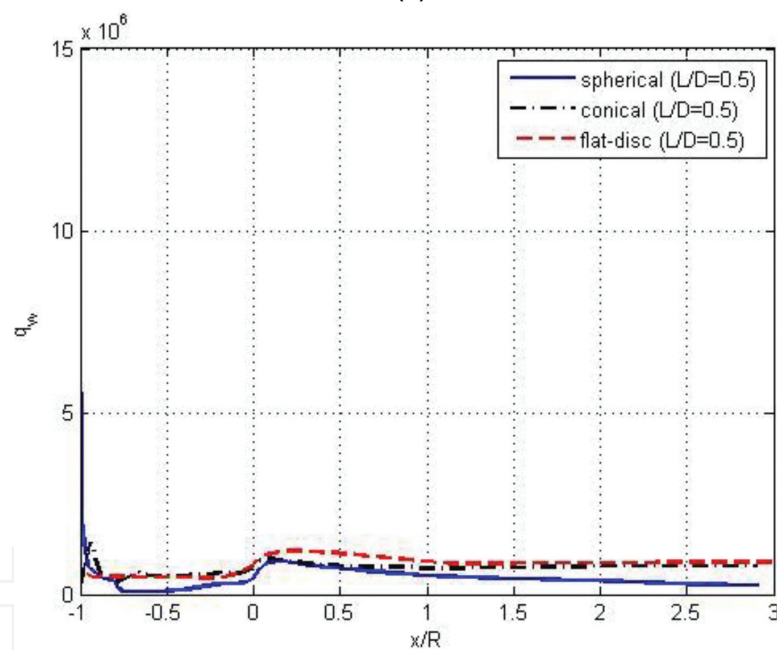
(b)

Figure 15. Variations of (a) pressure coefficient and (b) wall heat flux over the spiked blunt body.

5.4.3. Stagnation point heating and wall heat flux

The nose tip of a high-speed vehicle usually is hemi-spherically in shape. Consequently, a normal detached shock is formed in front of the stagnation point as depicted in **Figure 14(a)** which extends around the body as a curved oblique shock. The shock wave stands in front of the blunt body and forms a region of subsonic flow around the stagnation region and sonic line. The flow in the shock is at low subsonic speeds in the stagnation region and accelerates to sonic speeds in the shoulder region. For flat-nosed body, the detached bow shock wave of the

r/D_S	Cp	p/p_∞	cf	q_w, W/m^2
.00000E + 00	.14776E + 01	.38234E + 02	.42341E-05	.21158E + 06
.21500E-02	.15140E + 01	.39153E + 02	.11539E-03	.55592E + 07
.51000E-02	.15278E + 01	.39502E + 02	.68686E-04	.30266E + 07
.88500E-02	.15021E + 01	.38854E + 02	.55081E-04	.21678E + 07
.13500E-01	.14458E + 01	.37433E + 02	.49153E-04	.17160E + 07
.18950E-01	.13656E + 01	.35414E + 02	.45983E-04	.14250E + 07
.25200E-01	.12628E + 01	.32823E + 02	.43713E-04	.12121E + 07
.32300E-01	.11468E + 01	.29898E + 02	.40917E-04	.10449E + 07
.40250E-01	.10324E + 01	.27016E + 02	.36909E-04	.90977E + 06
.49000E-01	.92245E + 00	.24246E + 02	.33641E-04	.79750E + 06
.58600E-01	.82295E + 00	.21738E + 02	.32589E-04	.71001E + 06
.69000E-01	.71613E + 00	.19046E + 02	.33443E-04	.64654E + 06
.80250E-01	.59834E + 00	.16078E + 02	.35029E-04	.59998E + 06
.92300E-01	.48029E + 00	.13103E + 02	.35604E-04	.55673E + 06

Table 1. Variations of Cp, p/p_∞, cf and q_w over flat-face disk aerospike.

nose is particularly normal to the body axis. A compressible subsonic region is formed between the body and the shock which is a function of density ratio across the normal shock. The shock-detachment distance Δ and stagnation-velocity gradient K are essentially functions of density ratio across the normal shock [41, 42]. One of the areas of concern is the stagnation point heating of a spiked and unspiked body, when the incoming high-velocity flow is come to stagnation on the wall by a normal shock and adiabatically compression process. The problem now becomes finding out the heat flux in the vicinity of the stagnation point. It requires a solution of the entire flowfield from shock to the body.

The inviscid flowfield in the vicinity of the stagnation point is described in a fluid dynamics sense as the conversion of a unidirectional high-velocity stream by a normal shock wave into a high temperature subsonic layer, which is taken to be inviscid and incompressible [43]. The heat transfer rate is directly proportional to the enthalpy gradient on the body surface and square root of the velocity gradient, $(\beta = du_e/dx)_s$. The inviscid flowfield in the vicinity of the stagnation point is described as the conversion of the unidirectional, high-velocity flow by a normal shock wave into a high temperature subsonic flow. The enthalpy gradient is depended on the shape of the velocity profile in the boundary layer and by the variation of the air properties with temperature. Wall heat flux at the stagnation point of the blunt body can be calculated using the following expression of Fay and Riddell [48].

$$q_w = 0.763 \mathrm{Pr}^{-0.6} \sqrt{(\rho_e \mu_e K)} \sqrt{\left(\frac{\rho_w \mu_w}{\rho_e \mu_e}\right)} (h_e - h_w) \tag{5}$$

The stagnation point velocity gradient can be written as non-dimension parameter as $(K = \beta D/V_\infty)$, where D is the diameter of the blunt body. Newtonian flow and similarity

r/D_S	Cp	p/p_∞	Cf	q_w W/m²
0	1.8987	48.846	1.3293e-06	326,130
0.005	1.8974	48.814	5.7879e-05	1.4549e + 07
0.01	1.8906	48.643	2.7381e-05	7.2722e + 06
0.015	1.8798	48.372	1.6742e-05	4.8444e + 06
0.02	1.8669	48.046	1.1241e-05	3.6302e + 06
0.025	1.8529	47.694	7.9517e-06	2.9018e + 06
0.03	1.8386	47.333	5.8737e-06	2.4167e + 06
0.035	1.8244	46.974	4.5396e-06	2.0707e + 06
0.04	1.8102	46.616	3.6880e-06	1.8115e + 06
0.045	1.7957	46.253	3.1615e-06	1.6101e + 06
0.05	1.7807	45.873	2.8655e-06	1.4489e + 06
0.055	1.7642	45.458	2.7391e-06	1.3167e + 06
0.06	1.7449	44.972	2.7632e-06	1.2057e + 06
0.065	1.7221	44.396	3.0004e-06	1.1111e + 06
0.07	1.6957	43.731	3.5721e-06	1.0305e + 06
0.075	1.6573	42.765	4.8788e-06	960,610
0.08	1.5942	41.173	7.8607e-06	897,760
0.085	1.5726	40.629	1.0038e-05	853,270
0.09	1.3785	35.737	1.1276e-05	826,300
0.095	1.2663	32.910	1.0595e-05	855,090
0.1	0.5229	14.177	1.2575e-05	708,300

Table 2. Variations of Cp, p/p_∞, cf and q_w over hemispherical disk aerospike.

method [41, 43] methods do not take into consideration the finite compressibility that exists between the shock wave and the spike surface. Experiments were conducted by Boison et al. [49] in the supersonic wind tunnel to obtain the values of the stagnation point velocity gradient. The numerical analysis is able to take into consideration the compressibility effects in the subsonic region. The stagnation point stream-wise velocity gradient is given by the Newtonian impact theory, viz.,

$$\left(\frac{du_e}{dx}\right)_s = \frac{1}{R_N}\sqrt{\frac{2(\rho_2 - \rho_\infty)}{\rho_2}} \tag{6}$$

It is important to mention here that the sphere shows the greatest change in velocity gradient as compared to the flat disk. The magnitude of the stagnation-velocity gradient indicates the maximum heat transfer rate. The disk or flat plate with free streamlines will experience the lowest stagnation wall temperature of blunt body. The value K is considered as 0.3 [50]. The hemispherical aerospike exhibits the significant changes in the magnitude of K as compared to the flat disk aerospike. The magnitude of the K also indicates the

maximum heat transfer rate over the hemispherical disk. The computed values of the stagnation point heat flux $q_{w,s}$ are 0.556×10^7 W/m^2 and 1.45×10^7 W/m^2 for the flat-disk and the hemispherical disk aerospike, respectively. The $q_{w,s}$ calculated using Eq. (5) is 0.831×10^7 W/m^2 and 1.55×10^7 W/m^2 for the flat-disk and the hemispherical disk spike, respectively. The discrepancy is due to the value of the K. The value of K is difficult to calculate analytically and experimentally for the flat-face disk spike [50]. The expression for the stagnation point heat transfer [26] for a sphere is

$$\dot{q}_{w,s} = 1.83 \times 10^{-4} \left(\frac{\rho_w}{R_n} \right)^{0.5} V_\infty^3 \left[1 - \frac{H_w}{H_s} \right] \tag{7}$$

where R_N is nose radius in m, V_∞ is freestream velocity, H_w is the wall enthalpy and H_S the stagnation enthalpy. Experiments were carried out to evaluate the stagnation point velocity gradient.

5.5. Heat transfer measurements

Experiments [51] were carried out in shock tunnel to measure the heat flux on the blunt body attached with the hemispherical aerospike of L/D = 1.5 and 2.0 at zero angle of attack. **Figure 16** depicts the locations of heat transfer measurement. The shock tunnel consists of a shock tube divided into driver and driven sections, separated by a metallic diaphragm. The shock tube is connected to the wind tunnel portion by a convergent-divergent conical nozzle, test-section and dump tank separated by a diaphragm to obtain M_∞ = 6. The platinum sensors were fabricated by depositing a thin coating of platinum on the surface of Macor kept on the surface of the spiked model. The stagnation wall heat flux for the unspiked blunt body configuration was evaluated for the shock-tunnel conditions, using Fay and Riddell [48] equations. Surface heat flux on the basic body was obtained employing Lees [52] equations as
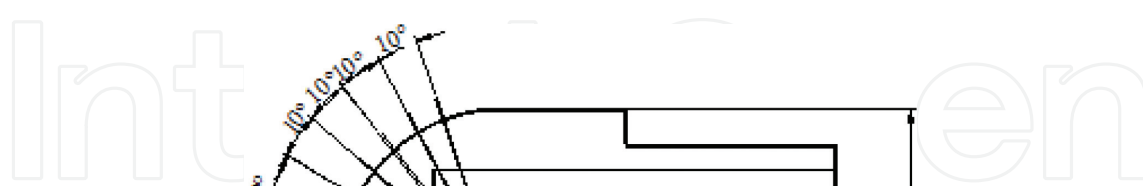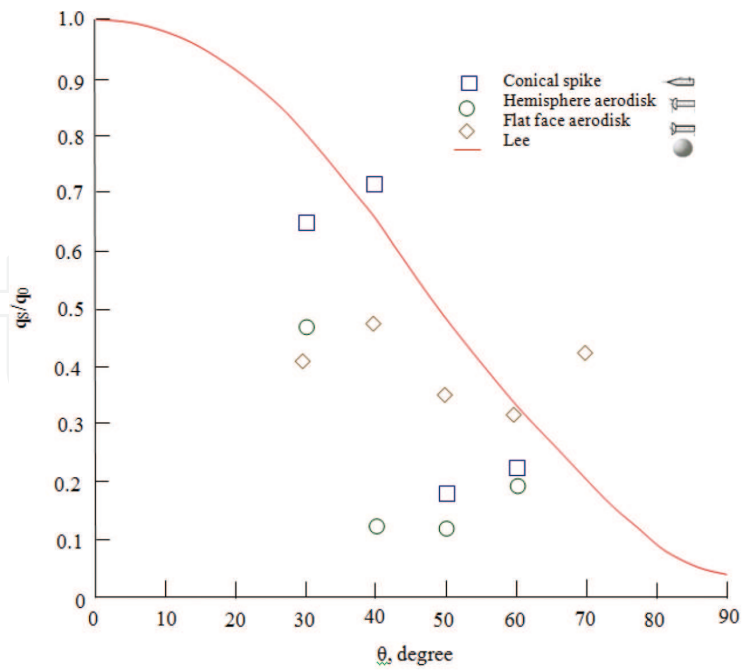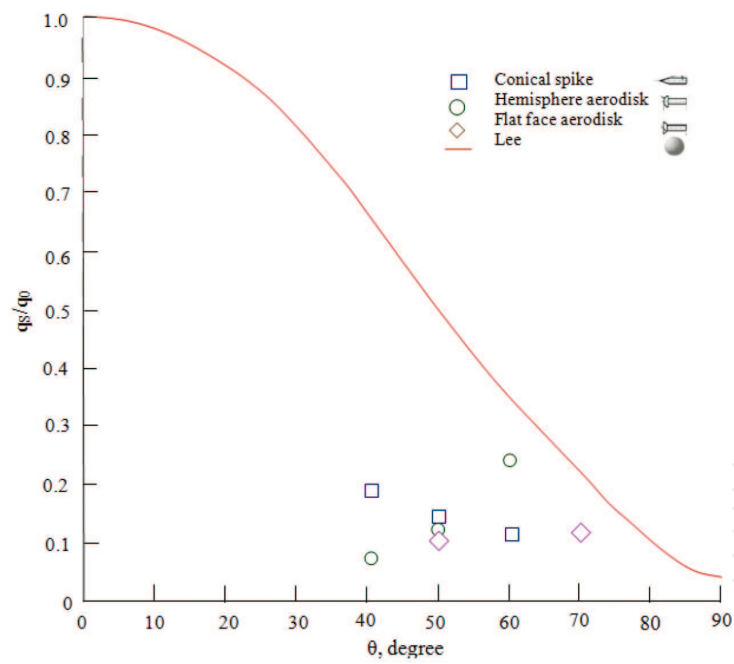

Figure 16. Locations of the heat transfer probes.

(a)

(b)

Figure 17. Variations of heat flux over the various spiked blunt body (a) L/D = 1.5 and (b) L/D = 2.0 at M_∞ = 6.0.

$$\frac{q_w}{q_S} = \frac{2\theta \sin\theta \left[\left\{ 1 - \frac{1}{\gamma M_\infty^2} \left(\cos^2\theta + 1 \right) \right\} \right]}{\sqrt{\left(1 - \frac{1}{\gamma M_\infty^2}\right)\left(\theta^2 - \frac{\theta \sin 4\theta}{2} + \frac{1 - \cos 4\theta}{8}\right) + \frac{4}{\gamma M_\infty^2}\left(\theta^2 - \theta \sin 2\theta + \frac{1 - \cos 2\theta}{2}\right)}} \tag{8}$$

The wall heat flux values are non-dimensionlised with the stagnation heat flux value. The temperature variations on the model surface that can be recorded using platinum thin film gauge can be used to find the heat transfer rate to the model by using the following expression [53]:

$$q(t) = \frac{\sqrt{k\rho C_p}}{2\sqrt{\pi}} \left[\frac{2T(t)}{\sqrt{t}} + \int_0^t \frac{T(t) - T(\tau)}{(t - \tau)^{3/2}} d\tau \right] \tag{9}$$

Evaluate above equation by applying approximate numerical schemes. Numerical methods involve division of the time interval (0, t) into a finite number of increments and the evaluation of the integrand at each of the division points. The heat flux over the basic configuration with and without spiked for a fixed L/D of 1.5 and 2.0 is shown in **Figure 17**. It is seen that for the basic body with spike the heat flux values is lower than the basic body without spike. Except the conical aerospike, all other spike configurations result in lower heat flux values than the basic body alone. For this length also, the spikes could reduce the heat flux on the basic body substantially, as seen from these results.

6. Conclusions

The flowfield around a forward facing a hemispherical and a flat disk spike attached to blunt-nosed body has been numerically simulated at high speeds at zero angle of attack. The flow visualizations were done using the velocity vector and contour plots in order to analyze the influence of the shape of the spike on the drag reduction and wall heat flux. The formation of the bow shock wave is observed over the unspiked and spiked blunt body. Different flow separation zones depend on the shape of the spike attached to the blunt body. The stand-off distances of the bow shock wave for the hemispherical and the flat aerospike are compared with the analytical solutions and are seen in good agreement. The variations of surface pressure, the skin friction coefficient and the wall heat flux along the surface of the spike facing the flow direction is significantly influenced by the geometrical shape of the spike. The density and pressure ratio and the heat flux at the stagnation point are computed and compared with the analytical results. The numerical analysis delineates complete flowfield information over the unspiked and the spiked blunt-body surface including the bow shock, shock stand-off distance shock, sonic line and stagnation point velocity gradient.

Nomenclature

C_f skin friction coefficient

C_p pressure coefficient

D cylinder diameter

L	length of the spike
M	Mach number
q	heat flux
p	pressure
R_N	radius of the spherical body
s	distance along the surface of the spike
T	temperature
t	time
x, r	coordinate direction
γ	ratio of specific heats
ρ	density
τ	dummy line variable
Δ	shock stand-off distance

Subscripts.

e	edge of the boundary layer
o	stagnation
w	wall
∞	freestream condition

Author details

Rakhab Chandra Mehta

Address all correspondence to: drrakhab.mehta@gmail.com

Department of Aeronautical Engineering, Noorul Islam Center for Higher Education, Noorul Islam University, Kumaracoil, India

References

[1] Takovitskii SA. Analytical solution in the problem of constructing axisymmetric noses with minimum wave drag. Fluid Dynamics. 2005;**41**(2):308-312

[2] Eggers AJ, Meyer M, Resniko D, Dennis H. Bodies of Revolution Having Minimum Drag at High Supersonic Airspeeds. Moffett Field, USA, NACA TR-1306: Ames Research Laboratory; 1957

[3] Allen HJ, Eggers AJ. A Study of the Motion and Aerodynamic Heating of Ballistic Missiles Entering the Earth's Atmosphere at High Supersonic Speeds. Moffett Field, USA, NACA-TR 1381: Ames Research Laboratory; 1958

[4] Yamamoto Y, Yoshioka M. CFD and FEM coupling analysis of OREX aero-thermodynamic flight data. 29th AIAA Thermophysics Conference, June 19–22, 1995, San Diego, California, USA, AIAA 95–2087

[5] Kovalev V, Yakuchikov A. Simulation of hydrogen adsorption in carbon nanotube arrays. Acta Astronatica. 2011;**68**:681-685

[6] Tret'yakov PK, Garanin AF, Grachev GN, Krainev VL, Ponomarenko AG, Tishchenko VN, Yakolec VI. Control of supersonic flow around bodies by means of high-power recurrent optical breakdown. Physics-Doklady. 1996;**41**(11):566-567

[7] Kim J-H, Matsuda A, Sakai T, Sasoh A. Wave drag reduction with acting spike induced by laser-pulse energy deposition. AIAA Journal. 2011;**49**:2076-2078

[8] Schülein E, Zheltovodov AA, Pimonov EA, Loginov MS. Experimental and numerical modeling of the bow shock interaction with pulse-heated air bubbles. International Journal Aerospace Innovation. 2010;**2**(3):183-205

[9] Schülein E, Zheltovodov A. Effects of steady flow heating by arc diskharge upstream of non-slender bodies. Shock Waves. 2011;**24**(4):383-390

[10] Artem'ev VI, Bergel'son VI, Nemchinoy TI, Orlova VA, Smirnov VM, Khazins VM. Change of regime in supersonic flow past an obstacle preceded by a thin channel of reduced density. Fluid Dynamics. 1989;**24**(5):779-784

[11] Meyer B, Nelson HF, Riggins DW. Hypersonic drag and heat-transfer reduction using a forward-facing jet. Journal of Aircraft. 2001;**38**(4):680-686

[12] Eghlima Z, mansour K, Fardipour K. Heat transfer reduction using combination of spike and counter flow jet on blunt body at high Mach number flow. Acta Astronautica. 2018; **143**:92-104

[13] Finley PJ. The flow of a jet from a body opposing a supersonic freestream. Journal of Fluid Mechanics. 1966;**26**(2):337-368

[14] Gordeev VP, Krasilnikov AV, Lagutin VI, Otmennikov VN. Experimental study of the possibility of reducing supersonic drag by employing plasma technology. Fluid Dynamics. 1996;**31**(2):313-317

[15] Shang JS. Plasma injection for hypersonic blunt-body drag reduction. AIAA Journal. 2002;**40**(6):1178-1186

[16] Fomin VM, Maslov AA, Malmuth ND, Fomichev VP, Shashkin AP, Korotaeva TA, Shiplyuk AN, Pozdnyakov GA. Influence of a counter flow plasma jet on supersonic blunt-body pressures. AIAA Journal. 2002;**40**(6):1170-1177

[17] Ladoon DW, Schneider SP, Schmisseur JD. Physics of a supersonic forward-facing cavity. Journal of Spacecraft and Rockets. 1998;**35**(5):626-632

[18] Schnepf C, Wysocki O, Schülein E. Wave drag reduction due to self-aligning aerodisk. Progress in Flight Physics. 2015;**7**:475-488

[19] Hayashi K, Aso S, Tani, Y: Numerical study of thermal protection system by opposing jet. 43rd AIAA Aerospace Sciences Meeting and Exhibit, Reno, Nevada, USA, 2005; AIAA 2005–188

[20] Georgievskii PY, Levin VA. Control of the flow past bodies using localized energy addition the supersonic oncoming flow. Fluid Dynamics. 2003;**38**(5):794-805

[21] Knight D, Kolesnichenko YF, Brovkin V, Khmara D. High speed flow control using microwave energy deposition. 16th Australasian Fluid Mechanics Conference, Gold Coast, Australia; Dec. 2007

[22] Reggins D, Nelson HF, Johnson E. Blunt-body wave drag reduction using focused energy deposition. AIAA Journal. 1999;**47**(4):460-467

[23] Liu Y, Jiang Z. Concept of non-ablative thermal protection system for hypersonic vehicles. AIAA Journal. 2013;**51**(3):584-590

[24] Motoyama N, Mihara K, Miyajima R, Watanuki T, Kubota H. Thermal protection and drag reduction with use of spike in hypersonic flow, AIAA/NAL-NASDA-ISAS. AIAA 2001–1828; 2001

[25] Ahmed MYM, Qin N. Recent advances in the aerothermodynamics of spiked hypersonic vehicles. Progress in Aerospace Science. 2011;**47**(6):425-449

[26] Tauber, ME: A review of high speed, convective, heat transfer computational methods. Ames Research Laboratory, Moffett Field, USA, NASA TP-2914, July 1989

[27] Wang Z-G, Sun X-W, Huang W, Li S-B, Yan L. Experimental investigation on drag and heat flux reduction in supersonic/hypersonic flows: A review. Acta Astronautica. 2016; **129**:95-110

[28] Kalimuthu R, Mehta RC, Rathakrishnan E. Experimental investigation on spiked body at hypersonic flow. The Aeronautical Journal. 2008;**112**(1136):593-598

[29] Mehta RC. Numerical simulation of the flowfield over conical, disk and flat spiked body at Mach 6. The Aeronautical Journal. 2010;**114**(1154):225-236

[30] Mehta RC. Numerical heat transfer study around a spiked blunt-nose body at Mach 6. Heat and Mass Transfer. 2013;**49**:485-496

[31] Mehta RC. Numerical heat transfer study over spiked blunt bodies at Mach 6.8. Journal of Spacecraft and Rockets. 2000;**37**(5):700-703

[32] Bogdonov SM, Vas IE. Preliminary investigations of spiked bodies at hypersonic speeds. Journal of Aerospace Sciences. 1959;**26**(2):65-74

[33] Fujita M, Kubota H. Numerical simulation of flowfield over a spiked blunt nose. Computational Fluid Dynamics Journal. 1992;**1**(2):187-195

[34] Yamauchi M, Fujjii K, Tamura Y, Higashino F. Numerical investigation of hypersonic flow around a spiked blunt body. AIAA Paper 93-0887; 1993

[35] Blazek J. Computational Fluid Dynamics: Principles and Applications. 1st ed. Oxford, UK: Elsevier Science Ltd; 2001

[36] Jameson A, Schmidt W, Turkel E. Numerical simulation of Euler equations by finite volume methods using Runge-Kutta time-stepping schemes. AIAA paper 81–1259; 1981

[37] Mehta RC. Isoperimetric finite element method to generate structured grid for numerical flow simulation. Journal of Aerospace Sciences and Technologies. 2017;**69**(4):588-596

[38] Mehta RC, Jayachandran T. Navier-stokes solution for a heat shield with and without a forward-facing spike. Computers and Fluids. 1997;**26**(7):741-754

[39] Mehta RC. Heat transfer study of high speed flow over a spiked blunt body. International Journal of Numerical Methods for Heat and Fluid Flow. 2000;**10**(7):750-769

[40] Probstein RF. Inviscid flow in the stagnation region of very blunt-nosed bodies at hypersonic flight speeds. WADC–TN 56-395; Sept. 1956

[41] Ames Research Staff. Equations, Tables and Charts for Compressible Flow. Moffett Field, USA, NACA report 1135: Ames Research Laboratory. p. 1953

[42] Liepmann HW, Roshko A. Elements of Gas Dynamics. 1st South Asian ed. New Delhi: Dover Publications Inc; 2007

[43] Truitt RW. Hypersonic Aerodynamic. New York, USA: Ronald Press Co.; 1959

[44] Hayer WD, Probstein RF. Hypersonic Flow Theory. New York: Academic Press; 1959

[45] Frank W, Zierep J. Schallnahe überschallströmung um rotationssymmetrische körper. Acta Mech. 1974;**19**:277-287

[46] Stilp, A: Strömungsuntersuchungen an Kgeln mit tranonischen und supersonischen Geschwidigkeiten in Luft und Frigen-Luftgemischen Bericht Nr. 10.65, Fckerstrasse 4, Germany; 1965

[47] Van Dyke MD, Gordon HD. Supersonic flow past a family of blunt axisymmetric bodies. NASA TR-R 1; 1959

[48] Fay JA, Riddell FR. Theory of stagnation point heat transfer in dissociated air. Journal of Aeronautical Sciences. 1958;**25**:73-85

[49] Boison JC, Curtiss HA. An experimental investigation of blunt body stagnation point velocity gradient. ARS Journal. 1959;**29**(2):130-135

[50] White FM. Viscous Fluid Flow. 2nd ed. Singapore: McGraw Hill International Edition; 1991

[51] Kalimuthu R. Experimental Investigation of Hemispherical Nosed Cylinder with and without Spike in a Hypersonic Flow. Ph. D. Thesis. Kanpur, India: Department of Aerospace Engineering, Indian Institute of Technology; April 2009

[52] Lees L. Laminar heat transfer over blunt-nosed bodies at hypersonic flight speeds. Jet Propulsion. 1956;**26**(4):259-269

[53] Cook WJ, Felderman EJ. Reduction of data from thin-film heat-transfer gages: A concise numerical technique. AIAA Journal. 1966;**4**(4):561-562